

Observation of optical gyromagnetic properties in a magneto–plasmonic metamaterial

Weihaoyang,^{1§} Qing Liu,^{2§} Hanbin Wang,^{3§} Yiqin Chen,^{2§} Run Yang,¹ Shuang Xia,¹ Yi Luo,³ Longjiang Deng,¹ Jun Qin,^{1*} Huigao Duan,^{2*} and Lei Bi^{1*}

¹National Engineering Center of Electromagnetic Radiation Control Materials School of Electronic Science and Engineering, University of Electronic Science and Technology of China, Chengdu, China, 610054

²College of Mechanical and Vehicle Engineering, Hunan University, Changsha 410082, China

E-mail: qinjun@uestc.edu.cn, duanhg@gmail.com, bilei@uestc.edu.cn

§ These authors contributed equally

Metamaterials with artificial optical properties have attracted significant research interest. In particular, artificial magnetic resonances in non-unity permeability tensor at optical frequencies in metamaterials have been reported. However, only non-unity diagonal elements of the permeability tensor have been demonstrated to date. A gyromagnetic permeability tensor with non-zero off-diagonal elements has not been observed at the optical frequencies. Here we report the observation of gyromagnetic properties in the near-infrared wavelength range in a magneto–plasmonic metamaterial. The non-zero off-diagonal permeability tensor element causes the transverse magneto-optical Kerr effect (TMOKE) under s-polarized incidence that otherwise vanishes if the permeability tensor is not gyromagnetic. By retrieving the permeability tensor elements from reflection, transmission, and TMOKE spectra, we show that the effective off-diagonal permeability tensor elements reach the 10^{-3} level at the resonance wavelength (~ 900 nm) of the splitting resonators that is at least two orders of magnitude higher than that of

magneto-optical materials at the same wavelength. The artificial gyromagnetic permeability is attributed to the change in the local electric field direction modulated by the split-ring resonators. Our study demonstrates the possibility of engineering the permeability and permittivity tensors in metamaterials at arbitrary frequencies, thereby promising a variety of applications of next-generation nonreciprocal photonic devices, magneto-plasmonic sensors, and active metamaterials.

Metamaterials have attracted considerable research interest in the past two decades because of their artificial electromagnetic properties, facilitating the realization of left-handed materials¹⁻³, invisible cloaking^{4,5}, and superlens^{6,7}. According to Landau and Lifshitz, the magnetic susceptibility χ_m vanishes at optical frequencies in conventional materials, that is, $\mu = 1$ ⁸. Therefore, the realization of optical magnetism with $\mu \neq 1$ and even $\mu < 0$ is of particular interest. Nanostructures including split-ring resonators⁹⁻¹¹, cut-wire pairs¹², dielectric/metal multilayer metamaterials^{13,14}, dielectric core-metal nanoparticle “satellite” nanostructures^{15,16}, and all dielectric resonators^{17,18} have emerged due to the realization of optical magnetism in recent years. Strong magnetic properties are observed at optical frequencies, leading to the realization of hyperlenses¹⁹, topological transitions²⁰, and interface-bound plasmonic modes^{21,22}. However, so far, only the non-unity diagonal component of the μ tensor has been demonstrated. The off-diagonal components of μ are trivial. Can gyromagnetic properties be realized at optical frequencies^{23,24}? Answering this question will allow the manipulation of ϵ and μ tensors in metamaterials and facilitate realizing novel metamaterials with bi-gyrotropic

properties at optical frequencies.

Magneto-optical (MO) materials usually show non-zero off-diagonal ϵ components at optical frequencies that are also called gyroelectric materials. However, the μ remains 1 owing to a mismatch of the low Larmor precession frequency of electron spins with the incident electromagnetic field frequency. Therefore, tensorial μ or even bi-gyrotropic properties (both gyroelectric and gyromagnetic) in MO materials has been pursued for a long time. In the 1950-1960s, gyromagnetic properties were measured in materials such as yttrium iron garnet (YIG) or Fe at optical frequencies. The transverse magneto-optical Kerr effect (TMOKE) under s-polarized incidence was measured that was nontrivial only if the material was gyromagnetic rather than gyroelectric. The off-diagonal tensor elements for YIG and Fe were measured to be at most 10^{-5} at optical frequencies²⁵, justifying the argument proposed by Landau and Lifshitz. In recent years, with the development of plasmonics and optical frequency metamaterials, magneto-plasmonic devices and MO metamaterials have been developed. These devices show significantly enhanced MO properties in metals, oxides, and 2D materials, thereby promising opportunities for the development of next-generation nanophotonic devices²⁶⁻³¹. However, almost all MO nanophotonic devices and metamaterials reported so far are limited to the manipulation of the ϵ tensor. Optical-frequency gyromagnetic metamaterials are still lacking.

In this study, we report the observation of gyromagnetic properties at near-infrared wavelengths in a magneto-plasmonic metamaterial. Using a classical Au split-ring resonator (SRR) structure on top of an MO thin film Ce-doped YIG (Ce:YIG), we

demonstrate s-polarized and p-polarized TMOKE in the hybridized MO-SRR metamaterial. Employing the transfer matrix methods, we demonstrate the off-diagonal element of μ reaching the 10^{-3} level at ~ 900 nm wavelength that is at least two orders of magnitude higher than that of Ce:YIG thin films at the same wavelength. The microscopic mechanism of the emergent gyromagnetic property is attributed to the local electric/magnetic field direction modulated by the metamaterial nanostructure, underscoring a general strategy of introducing gyromagnetic properties in optical frequency metamaterials. Our study demonstrates the possibility of manipulating the ϵ and μ tensors by hybridizing metamaterials and gyrotropic materials, providing a new degree of freedom to manipulate electromagnetic waves using metamaterials.

Device configuration and operation mechanism. The hybrid MO-SRR metamaterial is composed of periodic Au SRR on Ce:YIG/YIG bilayer films, deposited on a silicon substrate, as shown in Fig. 1a, b. The Ce:YIG and YIG thin films are dielectric and transparent MO materials with $n = 2.3$ and $n = 2.1$, respectively, in the near-infrared wavelength range²⁶. A linearly polarized light is obliquely incident onto the metamaterial with s- or p-polarization. The applied magnetic field is perpendicular to the plane of incidence (Voigt configuration). Under s-polarized incidence, the electric field is parallel to the SRR gap. The incident electromagnetic wave can couple into both the magnetic and electric resonance modes²⁷. Fig. 1b shows a schematic diagram of the metamaterial unit cell. The values of each length in the design are $g = 150$ nm, $q = t = 60$ nm, and $l = 105$ nm. The period p is 350 nm, and the thickness of Au is 35 nm. The

thicknesses of the Ce:YIG and YIG films are 70 nm and 50 nm, respectively, as confirmed using cross-sectional scanning electron microscopy (SEM) images. The top-view SEM image in Fig. 1c shows the geometrical morphology of the device with a zoomed-in figure showing one of the SRRs. Compared to the sizes of the design, the experimental results are identical except for the rounded corners of the SRR that is inevitable because of the lift-off process.

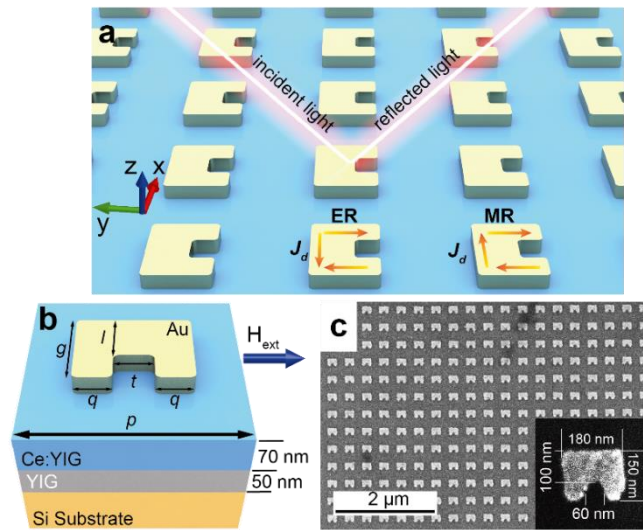


Fig. 1| Schematic and geometric morphology of the device. **a**, Schematic diagram of the MO-SRR metamaterial. The displacement current \mathbf{J}_d for both the electric resonance (ER) and magnetic resonance (MR) modes are shown. **b**, Schematic of a unit cell of the MO-SRR metamaterial with an Au-SRR on top of the Ce:YIG film (blue), YIG film (gray), and silicon substrate (Orange). **c**, SEM images of the MO-SRR metamaterial.

Transmission, reflection spectrum, and mode analysis. We simulated the transmission and reflection spectra of the device using the commercial software COMSOL Multiphysics based on the finite element method (FEM). In the case of s-

polarization with an incident angle of 45° , as shown in the inset of Fig. 2a, we can observe two resonant peaks or dips at 890 nm and 1350 nm wavelength for the reflection or transmission spectrum, respectively. The near-field distributions at the interface between the SRR and the Ce:YIG film in the X-Y plane are shown in Fig. 2b-e. First, at 890 nm wavelength, the amplitude of the electric field is almost concentrated at the top corner of the SRR and the electric field vector is along the x-direction, corresponding to the characteristics of the localized surface plasmon resonance, as shown in Fig. 2b. In Fig. 2c, the magnetic field is mainly concentrated at the edge of the horizontal top and two vertical arms, resulting from the circulating electric field at the edge. Therefore, the resonance at 890 nm corresponds to the electric resonance^{28,29}. At a wavelength of 1340 nm, the electric field is concentrated at the corners of the bottom short arms. The electric field vectors circulate around the gap, leading to an enhanced normal magnetic field in the gap area, as shown in Fig. 2d and e. Therefore, the resonance at 1340 nm corresponds to the magnetic resonance (LC resonance)^{28,30}. In the case of p-polarized incidence, the electric field has y- and z-components perpendicular to the gap. Therefore, only an electric resonance at ~ 990 nm can be excited, as shown in Fig. 2f. The electric resonance of the two vertical arms can be coupled through the horizontal top arm, leading to red-shifted symmetric and blue-shifted antisymmetric coupling modes. However, the antisymmetric mode is a dark mode that cannot be excited by symmetry protection³¹. From the electric and magnetic field distributions, we observe the electric field concentrated at the corners of the two vertical arms and the magnetic field edged at the two arms,

corresponding to symmetric coupled electric resonance, as shown in Fig. 2g and h.

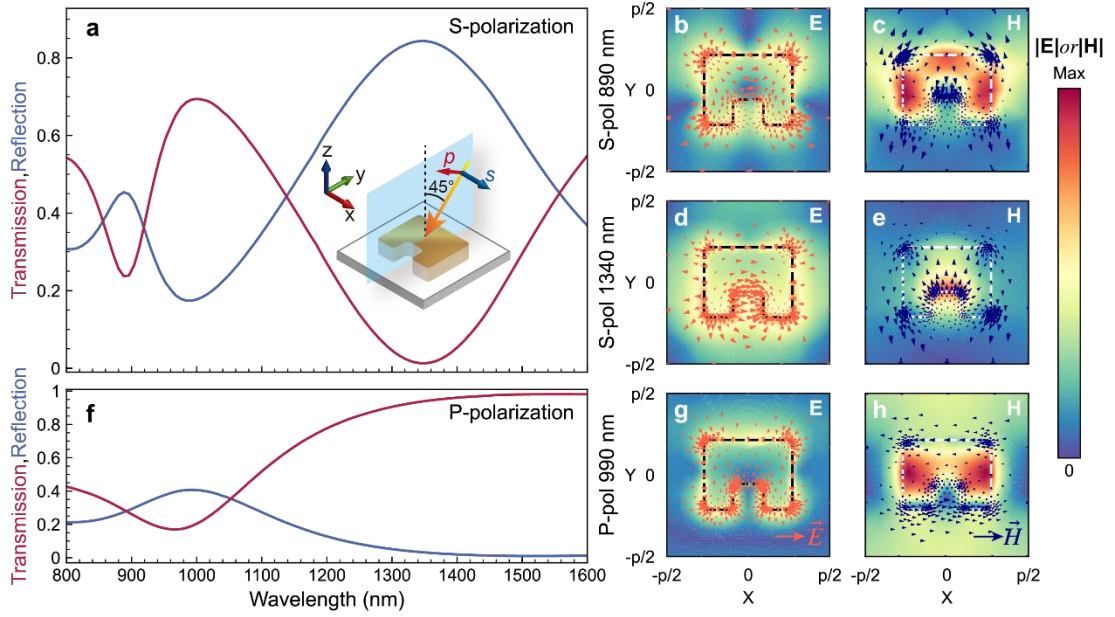


Fig. 2| Optical properties and near-field analysis. **a**, Transmission and reflection spectra under s-polarized incidence with an incident angle of 45°. **b**, Electric field and **c**, Magnetic field distributions under s-polarized incidence at 890 nm wavelength. **d**, Electric field and **e**, Magnetic field distributions under s-polarized incidence at 1340 nm wavelength. **f**, Transmission and reflection spectra under p-polarized incidence with an incident angle of 45°. **g**, Electric field and **h**, Magnetic field distributions under p-polarized incidence at 990 nm wavelength.

S-polarized TMOKE. The permittivity tensor of Ce:YIG and YIG in the Voigt configuration shown in Fig. 1a is

$$\hat{\varepsilon} = \begin{bmatrix} \varepsilon_0 & 0 & 0 \\ 0 & \varepsilon & -j\gamma \\ 0 & j\gamma & \varepsilon \end{bmatrix} \quad (1)$$

where ε_0 and ε are the diagonal elements, and γ is the off-diagonal elements attributed to the MO effect. It can be directly observed from the above equation that the MO effect

would vanish in planar MO films for s-polarized light with electric field along the x -direction. This is because the E_x -induced displacement in the MO material does not couple with γ . Furthermore, if the s-polarized TMOKE is non-zero, the $\hat{\mu}$ tensor of the metamaterial must have nontrivial off-diagonal elements owing to the incident H_y and H_z field components. We experimentally measured the reflection and TMOKE spectra under s-polarization for both the Ce:YIG/YIG bilayer films and the MO-SRR metamaterial using a spectroscopic ellipsometer (see Methods), as shown in Fig. 3. Fig. 3a shows the measured reflection spectra for different incident angles from 45° to 70° . (The maximum range of our ellipsometer is 45 - 75° .) We can observe two peaks at the wavelengths of ~ 890 nm and ~ 1340 nm, corresponding to the electric resonance and magnetic resonance modes, respectively. The electric field vector distributions of the two resonance modes are shown in the inset of Fig. 3a. As the incident angle increases from 45° to 70° , the reflectance of both resonances increases. In Fig. 3b, we simulate the reflection spectra at different incident angles. The experimental results agree well with the simulation results. To measure the TMOKE spectra, we used a permanent magnet to apply a magnetic field (± 3 kOe) in-plane. By switching the poles of the magnet, the reflection spectra under positive and negative magnetic fields were measured. The definition of TMOKE is

$$TMOKE = 2 \frac{R_{p/s}(H+) - R_{p/s}(H-)}{R_{p/s}(H+) + R_{p/s}(H-)} \quad (2)$$

where $R_{p/s}(H\pm)$ is the reflectance of the p-polarized (s-polarized) incidence under a positive or negative applied magnetic field. Remarkably, a clear s-polarized TMOKE reaching 3.0×10^{-3} is observed at the electric resonance wavelength, as shown in Fig.

3c that significantly contrasts the Ce:YIG thin film exhibiting zero TMOKE signal. In addition, the s-TMOKE of the Ce:YIG thin film is equal to zero for any incident angle. The shadow region of the spectra is the standard deviation of five consecutive TMOKE measurements. At the magnetic resonance wavelength, the amplitude of TMOKE is much weaker than that of electric resonance that originates from the lower MO effect of the Ce:YIG material (~ 0.2 times of that at the electric resonance) and higher reflectance of the device at a magnetic resonance wavelength of 1340 nm. We also measured the TMOKE spectrum in the incident angle range of $45\text{-}55^\circ$. The TMOKE signal decreases with incident angles that is consistent with the simulation results shown in Fig. 3d. The Ce:YIG thin film did not demonstrate s-TMOKE in both the experiments and simulations for different incident angles. According to our simulation, for this device, a maximum s-TMOKE of 2.7×10^{-3} may be observed at an incident angle of 30° (Supplementary Materials, Fig. S4).

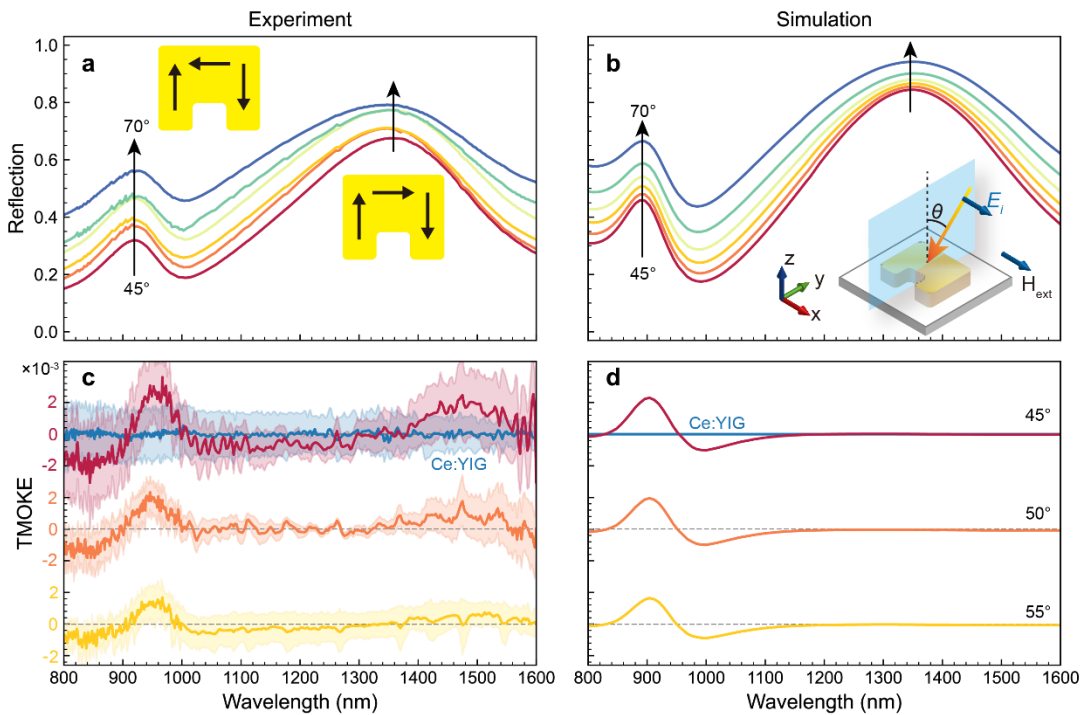


Fig. 3| Reflection and TMOKE spectra under s-polarized incidence. **a**, Measured and **b**, simulated reflection spectra of the MO–SRR metamaterial for incident angles ranging from 45° to 70° under s-polarized incidence. The inset of **a** shows the electric field directions for the electric and magnetic resonances. The inset of **b** shows the schematic of the incident plane and polarization. **c**, Measured and **d**, simulated TMOKE spectra of the MO–SRR metamaterial and the Ce:YIG thin film for different incident angles under s-polarized incidence.

P-polarized TMOKE. For p-polarization, only the gyrotropic permittivity tensor contributed to the TMOKE. The reflection and TMOKE spectra under p-polarized incidence are shown in Fig. 4. Because the electric field is perpendicular to the gap, only the electric resonance mode is excited at ~1000 nm, as shown in Fig. 4a. The reflectance decreases with the increasing incident angle owing to a weaker E_y component that excites the electric resonance. Fig. 4b shows the simulated reflection spectra with incident angles ranging from 45° to 70°. The experimental results agree well with the simulations. For 45° incidence, the TMOKE reaches 2×10^{-2} that is ~6.7 times higher than the s-polarized TMOKE, as shown in Fig. 4c. The maximum TMOKE shifts to a shorter wavelength relative to the reflection peak, owing to the contributions of the denominator (optical contribution) in equation (2). The larger noise of the spectra ranging from 1300 nm to 1600 nm is due to the lower signal-to-noise ratio of the ellipsometer at near-infrared wavelengths. Fig. 4d shows the simulated TMOKE spectra with incident angles varying from 45° to 55° that matches the experimental results excellently. The observed enhancement of p-polarized TMOKE at the electric

resonance is due to the localized surface plasmon resonance-enhanced gyroelectric properties of the MO thin film^{32,33}. Because the metamaterial exhibits both s-polarized TMOKE and p-polarized TMOKE in the 800-1000 nm wavelength range, it is called bi-gyrotropic^{34,35} that is extremely difficult to achieve in conventional magnetic materials owing to the large difference in the frequencies of the electric dipole transition and magnetic Larmor precession frequency of electrons.

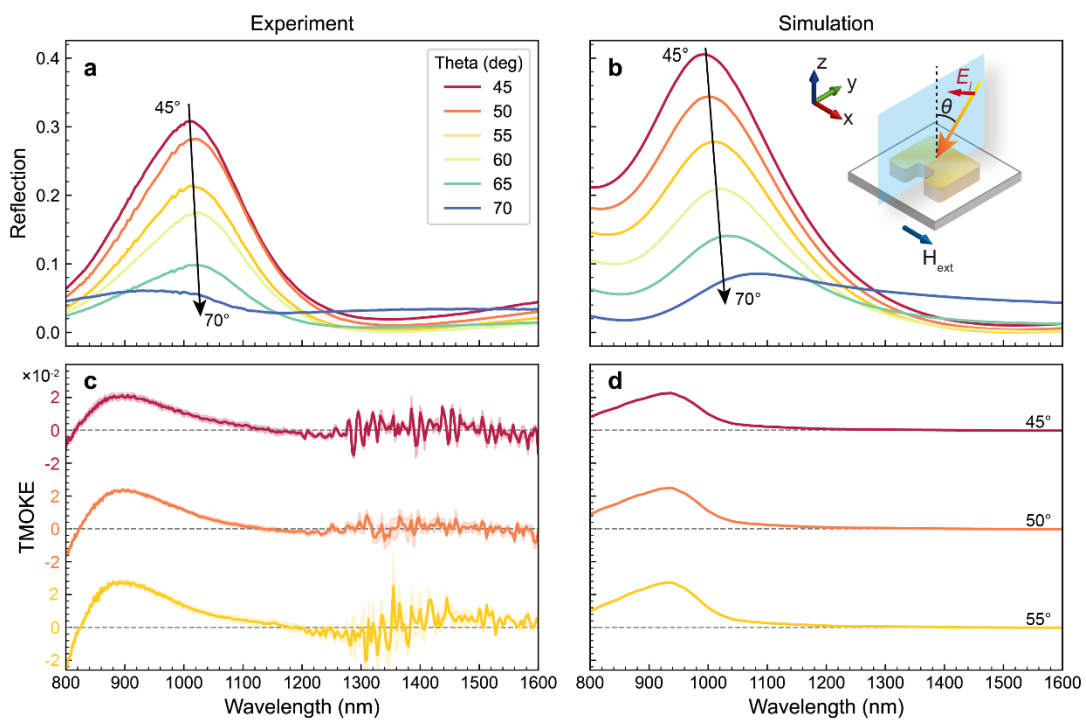


Fig. 4 | Reflection and TMOKE spectra under p-polarization. **a**, Measured and **b**, simulated reflection spectra of the MO-SRR metamaterial and the Ce:YIG thin film for different incident angles under p-polarized incidence. **c**, Measured and **d**, simulated TMOKE spectra of the MO-SRR metamaterial and the Ce:YIG thin film for different incident angles under p-polarized incidence.

Effective permittivity and permeability tensors. To obtain the effective ϵ and μ

tensors of the MO-SRR metamaterial, we retrieved the diagonal components of ϵ and μ tensors based on the 2×2 transfer matrix method (TMM) under glancing incidence. The MO-SRR metamaterial is equivalent to a homogeneous layer with an air cladding and silicon substrate. According to the standard 2×2 transfer matrices of multilayers³⁶, the transmission (T) and reflection (R) coefficients can be expressed by the permittivity and permeability of the material. By inverting T and R , one can obtain the diagonal components of ϵ and μ tensors (see details in Supplementary Materials Fig. S5).

Thereafter, we treat the MO effects as a perturbation of the ϵ and μ tensors upon applying a magnetic field. We used the 4×4 TMM to retrieve the off-diagonal elements by fitting the simulated TMOKE spectrum and phase difference of the reflection coefficient between positive and negative magnetic field. Based on this method, under s-polarization, we deduce the effective complex permittivity (ϵ_s) and permeability (μ_s) when the applied magnetic field is zero, as shown in Fig. 5a and 5b. Fig. 5a shows the real and imaginary parts of ϵ_s that implies resonant behavior at both the electric resonance and magnetic resonance wavelengths. In addition, the permittivity at the magnetic resonance is larger than the electric resonance, resulting from the near-zero transmittance at the magnetic resonance wavelength (see Fig. 2a). For μ_s , the trend is similar to that of ϵ_s , with magnetic response at both the electric resonance and magnetic resonance wavelengths³⁷. The MO contributions under s-polarization originate from the non-diagonal components of the permeability tensor that is defined as

$$\hat{\epsilon} = \begin{bmatrix} \mu_0 & 0 & 0 \\ 0 & \mu & -j\kappa \\ 0 & j\kappa & \mu \end{bmatrix} \quad (3)$$

where μ_0 is the vacuum permeability, and μ is the diagonal component of the permeability tensor without an applied magnetic field. κ is the MO permeability parameter. Fig. 5c shows the retrieved complex κ parameters. Both the real and imaginary parts of κ can reach 1.6×10^{-3} at the electric resonances. Similarly, the permittivity tensor can be determined employing the aforementioned method and process under p-polarization, as shown in Fig. 5d-5f. The resonant behaviors of both ε_p and μ_p are observed at the electric resonance wavelength. The non-diagonal components of permittivity γ approach 1.3×10^{-2} . To confirm the correctness of these parameters, we use the transfer matrix method to calculate the transmission, reflection, and TMOKE spectra using the equivalent material parameters that is consistent with the simulated TMOKE spectrum of the MO-SRRs. (see Supplementary Information, Fig. S6).

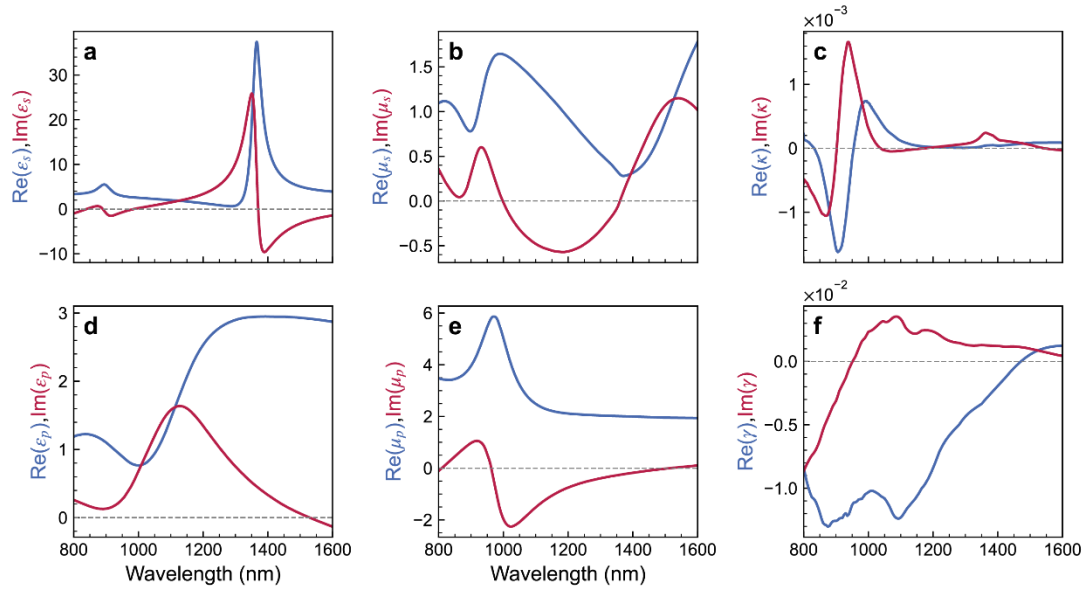


Fig. 5| Gyrotropic permeability and permittivity tensor of the MO-SRR metamaterials.

a, Diagonal components of the complex permittivity under s-polarization. **b**, Diagonal

components of the complex permeability under s-polarization. **c**, Off-diagonal components of the complex permeability tensor. **d**, Diagonal components of the complex permittivity under p-polarization. **e**, Diagonal components of the complex permeability under p-polarization. **f**, Off-diagonal components of the complex permittivity tensor.

The microscopic origin of the gyromagnetic properties of the MO-SRR metamaterial can be understood based on the mode profile in Fig. 2 and Fig. 3a, where the electric field (E_y) in both arms of the MO-SRR is orthogonal to the incident electric field direction (E_x) upon excitation of the resonance modes. This local change in the electric field direction causes a nontrivial magneto-optical effect according to equation (1), resulting in an s-polarized TMOKE. It should be noted that several recent experiments reported the observation of s-polarized TMOKE in magneto-nanophotonic devices^{38,39} that share similar microscopic mechanisms of local changes in electric field directions. From a metamaterial perspective, they are all optical gyromagnetic materials. Therefore, a general strategy to introduce optical gyromagnetic properties is to engineer the local electric field direction in magneto-nanophotonic devices, such as magneto-plasmonic metamaterials, MO waveguides, or all dielectric metasurfaces.

The above observation highlights the possibility of engineering the permittivity and permeability tensors in magnetic metamaterials or metasurfaces that enables new degrees of freedom to control electromagnetic wave propagation. For example, the realization of bi-gyrotropic materials allows controlling the transmission intensity/phase for both the electric and magnetic fields of the incident

electromagnetic wave by applying magnetic fields, offering a higher degree of freedom for polarization control in active metasurfaces. The bi-gyrotropic nature of the metasurfaces also enables independent design of the MO effects, such as TMOKE for p- and s-polarizations that may be used for the design of polarization-independent on-chip MO isolators or circulators⁴⁰, nonreciprocal metasurfaces for vectoral magnetic field sensing⁴¹, or biomedical sensing applications^{42,43}. Artificial ϵ or μ tensors can also significantly extend the frequency range of magneto-optical properties in conventional magnetic materials that are inherently tied to the band structure or magnetic properties of the material. For example, it is possible to realize strong gyromagnetic/gyroelectric properties in frequencies such as mid-infrared, long-wave infrared, or THz frequencies that are difficult to achieve in conventional magneto-optical materials, facilitating the development of nonreciprocal photonic devices in these frequency ranges.

Conclusions

In summary, we report the observation of optical gyromagnetic properties in an MO-SRR metamaterial in the near-infrared wavelength range. By measuring the TMOKE spectra under s- and p-polarizations, we demonstrate the bi-gyrotropic nature of the magneto-metamaterial. Using the 2×2 and 4×4 transfer matrix method, we determine the off-diagonal elements of μ reaching 1×10^{-3} , at least two orders of magnitude higher than MO thin-film materials at the same wavelength. A general strategy for local electric/magnetic field vector design in magnetic metamaterials is proposed for the realization of optical gyromagnetic or microwave gyroelectric properties. Our study

introduces a new degree of freedom in metamaterials that paves the way for engineering of the ϵ and μ tensor in advanced nanophotonic structures for nonreciprocal photonic devices, magneto-plasmonic sensors, and active metamaterial applications.

References

1. Pendry, J. B., Holden, A. J., Stewart, W. J. & Youngs, I. I. Extremely low frequency plasmons in metallic mesostructures. *Phys. Rev. Lett.* **76**, 4773-4776 (1996).
2. Pendry, J. B. Negative refraction makes a perfect lens. *Phys. Rev. Lett.* **85**, 3966-3969 (2000).
3. Shelby, R. A., Smith, D. R. & Schultz, S. Experimental verification of a negative index of refraction. *Science* **292**, 77-79 (2001).
4. Xu, H. X. *et al.* Polarization-insensitive 3D conformal-skin metasurface cloak. *Light Sci. Appl.* **10**, 75 (2021).
5. Zhang, F. *et al.* Phase-modulated scattering manipulation for exterior cloaking in metal-dielectric hybrid metamaterials. *Adv. Mater.* **31**, e1903206 (2019).
6. Chen, W. T. *et al.* A broadband achromatic metalens for focusing and imaging in the visible. *Nat. Nanotechnol.* **13**, 220-226 (2018).
7. Zhang, C. *et al.* A reconfigurable active acoustic metalens. *Appl. Phys. Lett.* **118**, 133502 (2021).
8. Landau, L., Lifshitz, E. & Pitaevski, L. *Electrodynamics of continuous media* Pergamon. *New York*, 224-233 (1960).
9. Wang, W., Yan, F. P., Tan, S. Y., Zhou, H. & Hou, Y. F. Ultrasensitive terahertz metamaterial sensor based on vertical split ring resonators. *Photonics Res.* **5**, 571-577 (2017).
10. Tsai, W. Y. *et al.* Second harmonic light manipulation with vertical split ring resonators. *Adv. Mater.* **31**, e1806479 (2019).
11. Kim, N. *et al.* Colossal terahertz field enhancement using split-ring resonators with a sub-10 nm gap. *ACS Photonics* **5**, 278-283 (2018).
12. Grigorenko, A. N. *et al.* Nanofabricated media with negative permeability at visible frequencies. *Nature* **438**, 335-338 (2005).
13. Papadakis, G. T., Fleischman, D., Davoyan, A., Yeh, P. & Atwater, H. A. Optical magnetism in planar metamaterial heterostructures. *Nat. Commun.* **9**, 296 (2018).
14. Verre, R., Yang, Z. J., Shegai, T. & Kall, M. Optical magnetism and plasmonic Fano resonances in metal-insulator-metal oligomers. *Nano Lett.* **15**, 1952-1958 (2015).
15. Véronique, M. *et al.* High optical magnetism of dodecahedral plasmonic meta-atoms. *Nanophotonics* **8**, 549-558 (2019).
16. Manna, U. *et al.* Selective induction of optical magnetism. *Nano Lett.* **17**, 7196-7206 (2017).
17. Kang, L., Bao, H. G. & Werner, D. H. Interference-enhanced optical magnetism

- in surface high-index resonators: a pathway toward high-performance ultracompact linear and nonlinear meta-optics. *Photonics Res.* **7**, 1296-1305 (2019).
18. Ginn, J. C. *et al.* Realizing optical magnetism from dielectric metamaterials. *Phys. Rev. Lett.* **108**, 097402 (2012).
 19. Lu, D. & Liu, Z. Hyperlenses and metalenses for far-field super-resolution imaging. *Nat. Commun.* **3**, 1205 (2012).
 20. Krishnamoorthy, H. N., Jacob, Z., Narimanov, E., Kretzschmar, I. & Menon, V. M. Topological transitions in metamaterials. *Science* **336**, 205-209 (2012).
 21. Elser, J. & Podolskiy, V. A. Scattering-free plasmonic optics with anisotropic metamaterials. *Phys. Rev. Lett.* **100**, 066402 (2008).
 22. Lezec, H. J., Dionne, J. A. & Atwater, H. A. Negative refraction at visible frequencies. *Science* **316**, 430-432 (2007).
 23. Liang, X., Xie, J. L., Deng, L. J. & Bi, L. First principles calculation on the magnetic, optical properties and oxygen vacancy effect of $Ce_xY_{3-x}Fe_5O_{12}$. *Appl. Phys. Lett.* **106**, 052401 (2015).
 24. Zhang, Y. *et al.* Enhanced magneto-optical effect in $Y_{1.5}Ce_{1.5}Fe_5O_{12}$ thin films deposited on silicon by pulsed laser deposition. *J. Alloys Compd.* **703**, 591-599 (2017).
 25. Krinchik, G. & Chetkin, M. V. Transparent ferromagnets. *Sov. Phys. Usp.* **12**, 307 (1969).
 26. Zvezdin, A. K. & Kotov, V. a. c. A. *Modern magneto-optics and magneto-optical materials.* (CRC Press, 1997).
 27. Rockstuhl, C. *et al.* Resonances of split-ring resonator metamaterials in the near infrared. *Appl. Phys. B: Lasers Opt.* **84**, 219-227 (2006).
 28. Katsarakis, N., Koschny, T., Kafesaki, M., Economou, E. N. & Soukoulis, C. M. Electric coupling to the magnetic resonance of split ring resonators. *Appl. Phys. Lett.* **84**, 2943-2945 (2004).
 29. Alù, A., Salandrino, A. & Engheta, N. Negative effective permeability and left-handed materials at optical frequencies. *Opt. Express* **14**, 1557-1567 (2006).
 30. Enkrich, C. *et al.* Focused-ion-beam nanofabrication of near-infrared magnetic metamaterials. *Adv. Mater.* **17**, 2547 (2005).
 31. Enkrich, C. *et al.* Magnetic metamaterials at telecommunication and visible frequencies. *Phys. Rev. Lett.* **95**, 203901 (2005).
 32. Belotelov, V. I. *et al.* Enhanced magneto-optical effects in magnetoplasmonic crystals. *Nat. Nanotechnol.* **6**, 370-376 (2011).
 33. Caballero, B., Garcia-Martin, A. & Cuevas, J. C. Hybrid magnetoplasmonic crystals boost the performance of nanohole arrays as plasmonic sensors. *ACS Photonics* **3**, 203-208 (2016).
 34. Krinchik, G. & Gushchin, V. Magneto-optical effect of change of electronic structure of a ferromagnetic metal following rotation of the magnetization vector. *JETP Lett.* **10**, 24 (1969).
 35. Amanollahi, M. & Zamani, M. Wide-angle giant transverse magneto-optical Kerr effect in a gyromagnetic superlens. *Opt. Lett.* **43**, 4851-4854 (2018).

36. Yeh, P. *Optical Waves in Layered Media*. (Wiley, 2005).
37. Linden, S. *et al.* Magnetic response of metamaterials at 100 terahertz. *Science* **306**, 1351-1353 (2004).
38. Ignatyeva, D. O. *et al.* All-dielectric magnetic metasurface for advanced light control in dual polarizations combined with high-Q resonances. *Nat. Commun.* **11**, 5487 (2020).
39. Xia, S. *et al.* Circular displacement current induced anomalous magneto-optical effects in high index Mie resonators. *arXiv preprint arXiv:2108.00615* (2021).
40. Yan, W. *et al.* Waveguide-integrated high-performance magneto-optical isolators and circulators on silicon nitride platforms. *Optica* **7**, 1555-1562 (2020).
41. Chen, S., Fan, F., He, X., Chen, M. & Chang, S. Multifunctional magneto-metasurface for terahertz one-way transmission and magnetic field sensing. *Appl. Opt.* **54**, 9177-9182 (2015).
42. Zhang, S. Y. *et al.* Metasurfaces for biomedical applications: imaging and sensing from a nanophotonics perspective. *Nanophotonics* **10**, 259-293 (2021).
43. Basiri, A. *et al.* Nature-inspired chiral metasurfaces for circular polarization detection and full-Stokes polarimetric measurements. *Light Sci. Appl.* **8**, 78 (2019).

Methods

Sample fabrication. The YIG (50 nm) and Ce:YIG (70 nm) films were deposited on a Si substrate via pulse laser deposition (PLD, TSST). The YIG film was first deposited using a 248 nm KrF excimer laser in a 5 mTorr oxygen ambient at 400 °C. The laser fluence was 3 J/cm², and the base pressure before deposition was 1 × 10⁻⁶ mTorr. After deposition, the film was cooled to room temperature in vacuum, followed by rapid thermal annealing in oxygen ambient (2 Torr) at 850 °C for 3 min, for crystallization. After YIG film crystallization, the Ce:YIG film was deposited in 10 mTorr oxygen ambient at 750 °C and cooled in the same oxygen ambient to room temperature at a rate of 5 °C /min.

The Au SRRs were fabricated via electron beam lithography (EBL, Raith 150-TWO), thermal evaporation, and lift-off process. First, a polymethyl methacrylate (PMMA) resist was spin-coated on the Ce:YIG film at a spin speed of 4000 rpm and

baked for 5 min at 180 °C on a hot plate. Thereafter, the nanostructure of the SRR was patterned via EBL with an accelerating voltage of 30 kV and an average dose of 270 $\mu\text{C}/\text{cm}^2$. After exposure, the samples were developed in a mixed solution of 3:1 isopropyl alcohol (IPA)/methyl isobutyl ketone for 1 min and rinsed in deionized water for 1 min. Subsequently, a layer of Au was deposited by thermal evaporation (Leybold, UNIVEX250) at room temperature. Finally, the sample was lifted off in an acetone solution with ultrasonic cleaning and rinsed in IPA.

Optical and magneto-optical simulation. The optical and magneto-optical responses of the metamaterials were simulated using commercial software based on the finite element method (COMSOL MULTIPHYSICS). Periodic boundary conditions were used to account for the periodic structure of the SRR. The polarization and incident angle of light are defined in the incident port. To avoid the effect of the scattered light, a perfectly matched layer was set at the top and bottom layers near the ports. The reflectance and transmittance spectra were calculated using the scattering parameters of COMSOL. For the permittivity of Au, we used the Drude model to fit the permittivity. The refractive index of YIG and permittivity tensor of Ce:YIG were obtained from a previous study²⁶. To obtain the TMOKE spectra, the reflectance spectra under positive and negative magnetic fields were simulated. The switching of the magnetic field direction was simulated as the sign change of the off-diagonal elements of the permittivity tensor.

TMOKE characterization. The TMOKE spectra were measured using a spectroscopic ellipsometer (J. Woollam RC2) in the wavelength range of 230-1690 nm. The incident angles can change from 45° to 75°. The ellipsometer equipped with two objective lenses can focus on a 100 μm \times 200 μm light spot at 45° incidence. The reflectance spectra under s- and p-polarization were obtained through a single measurement. To obtain the TMOKE spectra, a permanent magnet with a 3 kOe magnetic field was used to magnetize the sample in the Voigt geometry. By switching the magnetic field direction, the reflectance spectra were measured under positive and negative magnetic fields. The TMOKE spectra were obtained using equation (2).

Data availability

The data that support the findings of this study are available from the corresponding authors upon reasonable request.

Acknowledgements

The authors are grateful for support by the National Natural Science Foundation of China (NSFC) (Grant Nos. 51972044, 11574316, 52021001), Sichuan Provincial Science and Technology Department (Grant No. 2019YFH0154), Ministry of Science and Technology of the People's Republic of China (MOST) (Grant Nos. 2016YFA0300802, 2016YFA0401803, 2018YFE0109200), the Fundamental Research Funds for the Central Universities, and the Open-Foundation of Key Laboratory of Laser Device Technology, China North Industries Group Corporation Limited.

Author contributions

W. Y. performed the device design, metamaterial characterization and parameters retrieval. R. Y. deposited the magneto-optical thin films. Q. L. and Y. C. fabricated the SRRs nanostructures. S. X. conducted device characterization. J. Q., L. B., H. D., and L. D. supervised the research. All authors contributed to technical discussions and writing the paper.

Competing interests

The authors declare no competing interests.

Figure Legends

- **Fig. 1| Schematic and geometric morphology of the device.** **a**, Schematic diagram of the MO-SRR metamaterial. The displacement current J_d for both the electric resonance (ER) and magnetic resonance (MR) modes are shown. **b**, Schematic of a unit cell of the MO-SRR metamaterial with an Au-SRR on top of the Ce:YIG film (blue), YIG film (gray), and silicon substrate (Orange). **c**, SEM images of the MO-SRR metamaterial.
- **Fig. 2| Optical properties and near-field analysis.** **a**, Transmission and reflection spectra under s-polarized incidence with an incident angle of 45° . **b**, Electric field and **c**, Magnetic field distributions under s-polarized incidence at 890 nm wavelength. **d**, Electric field and **e**, Magnetic field distributions under s-polarized incidence at 1340 nm wavelength. **f**, Transmission and reflection

spectra under p-polarized incidence with an incident angle of 45° . **g**, Electric field and **h**, Magnetic field distributions under p-polarized incidence at 990 nm wavelength.

- **Fig. 3| Reflection and TMOKE spectra under s-polarized incidence.** **a**, Measured and **b**, simulated reflection spectra of the MO-SRR metamaterial for incident angles ranging from 45° to 70° under s-polarized incidence. The inset of **a** shows the electric field directions for the electric and magnetic resonances. The inset of **b** shows the schematic of the incident plane and polarization. **c**, Measured and **d**, simulated TMOKE spectra of the MO-SRR metamaterial and the Ce:YIG thin film for different incident angles under s-polarized incidence.
- **Fig. 4| Reflection and TMOKE spectra under p-polarization.** **a**, Measured and **b**, simulated reflection spectra of the MO-SRR metamaterial and the Ce:YIG thin film for different incident angles under p-polarized incidence. **c**, Measured and **d**, simulated TMOKE spectra of the MO-SRR metamaterial and the Ce:YIG thin film for different incident angles under p-polarized incidence.
- **Fig. 5| Gyrotropic permeability and permittivity tensor of the MO-SRR metamaterials.** **a**, Diagonal components of the complex permittivity under s-polarization. **b**, Diagonal components of the complex permeability under s-polarization. **c**, Off-diagonal components of the complex permeability tensor. **d**,

Diagonal components of the complex permittivity under p-polarization. ϵ ,

Diagonal components of the complex permeability under p-polarization. μ , Off-

diagonal components of the complex permittivity tensor.